Near-field optical study of mesoscopic Au periodic samples: Effect of the polarization and comparison between different imaging modes

L. Salomon,* C. Charbonnier, and F. de Fornel
Laboratoire de Physique de l'Université de Bourgogne, Groupe d'Optique de Champ Proche, CNRS (UPRESA 5027), Faculté des Sciences Mirande, Boîte Postale 47870, 21078 Dijon Cedex, France

P. M. Adam
Laboratoire de Nanotechnologie et d'Instrumentation Optique, Université de Technologie de Troyes, 12 rue M. Curie, Boîte Postale 2060 10010 Troyes, France

P. Guérin
Laboratoire de Métallurgie Physique, Bt. SP2MI, Université de Poitiers, Bd 3 Tlport 2, Boîte Postale 179, 86960 Futuroscope Cedex, France

F. Carcenac
Laboratoire de Microstructures et de Microléctronique, 196 Avenue H. Ravera, Boîte Postale 107, 92195 Bagneux Cedex, France
(Received 1 June 1999)

This paper presents a complete study, theoretical as well as experimental, of an electromagnetic field scattered by subwavelength metallic pads, allocated in a periodic manner on a silica substrate. The simulation of the far field and near field is obtained with the differential method. When the sample is illuminated in total internal reflection, the simulations show that the amplification of the electromagnetic field above the Au metallic pads depends on different parameters (wavelength, polarization of light, angle of incidence, and index of refraction). In this paper, we only consider the effect of the probe-to-sample distance and of the polarization of the illuminating light. As the experimental setup, we used the photon scanning tunneling microscope. If we compare these results with the calculations carried out with the dielectric pads, we show that the amplification is induced by the dielectric contrast between the metallic structures and their environment. Experimental results are presented in two different imaging modes. In the ''constant intensity'' mode, our experimental results are in excellent agreement with the simulations. Therefore, for a metallic sample analyzed in our experimental conditions, it validates the assumption that the signal detected is proportional to the square modulus of the electric field in the absence of the probe. We particularly show that if the polarization and the probe-to-sample distance are suitably chosen, dramatic localizations of the electromagnetic field are observed. We then present images obtained in the so-called ''two-wavelength'' mode, where two light sources illuminate the sample. The first beam is used for feedback regulation; it consequently allows a control of the tip motion, and permits us to determine the reference surface. By using such feedback regulation for this first beam, we are able to compare quantitatively the effect of the polarization on the field distribution of the second beam. The results are confirmed by the corresponding simulations.

I. INTRODUCTION

Submicron metal particles, i.e., with a size smaller than the wavelength of incident light are used[1] to investigate surface enhancement Raman spectroscopy and second-harmonic generation, as well as enhanced one- and two-photon absorption by adsorbed dyes. It is now widely accepted that these phenomena originate mainly in the excitation of surface-plasmon oscillations (SPO's) which enhance the local-field intensity near these metal particles.

Recently, several studies employing scanning near-field optical microscopes have been reported to investigate SPO's on metallic thin films. The photon scanning tunneling microscope (PSTM) has been used to measure the spatial extension of the SPO evanescent field,[2,3] and to image its lateral decay on a thin silver film in the visible range.[4] Localized SPO's on individual metal particles have been observed by coupling a PSTM and a scanning tunneling microscope.[5] The localization of optical modes in silver colloid fractal clusters have been investigated with the technique of the PSTM.[6] More recently, different studies has shown the role of surface inhomogeneities in the modification of the field emitted from the SPO's.[7,8]

In this paper, we mainly present results showing the effects of the polarization of the incident light on the near-field diffracted by a crossed grating of submicron gold pads. Several authors exploited the polarization contrast on metallic structures to improve the image contrast.[9–11] Our simulations show that, according to the polarization, the scattered near-field of the metallic pads is more or less confined near the edges of the pads. We present a comparison with the near-field close to dielectric pads.

Then we show, in the ''constant intensity'' mode, the role of the polarization of the incoming wave lighting the metallic pads, as well as the role of the probe-to-sample distance. We showed, in a previous paper,[12] that when the tip scans the

sample in the constant intensity mode, the amplitude of the vertical displacement of the probe is influenced by the value of the intensity detected by the fiber probe. Generally, for a strong value of the intensity (the probe is close to the sample), the amplitude of the vertical displacements of the fiber probe is relatively weak; on the other hand, for a weak value of the intensity (the probe is moved away from the sample), this amplitude increases. In order to compare the images obtained in the two directions of polarization of the illuminated light, we have carried out these measurements in the ''two-wavelength'' mode. This permits one to follow the isointensity lines issued from the first light source, which acts as a reference, while measurements with a second light source allow one to record the intensity of the electromagnetic field scattered by the sample and detected by the probe under variable illumination conditions.[3]

Section II is devoted to a description of the sample and the experimental setup used to analyze the electromagnetic field scattered by the sample. In Sec. III, we introduce the differential method in three dimensions, which allows us to obtain the exact solutions of Maxwell's equations when the sample is illuminated in total internal reflection (TIR). We present several remarks on the behavior of the intensity detected above the metallic pads in the ''constant height'' mode. We study the effects of the polarization, and of the probe-to-sample distance on the scattered intensity. We then compare the near-field diffracted by metallic and dielectric pads. In the next two sections we present our results, and we discuss the near-field above the pads when the polarization is in TE and TM modes for the two operating modes. Our conclusions are presented in Sec. VI.

II. DESCRIPTION OF THE SAMPLE AND EXPERIMENTAL SETUP

The sample studied is a crossed grating of gold structures on a glass slide 1 mm thick; the index of refraction is $n_1 = 1.458$. In this work, we have chosen a grating where the Au metallic pads are well separated to reduce the weight of the propagating modes diffracted by the sample. The separation between two metallic pads is equal to 3 μm in each direction. Each pad is parallelepipedic with dimensions: 300×300 nm^2 and 50 nm. The sample is obtained by reaction ion etching, and it is fabricated with an incertainty of 5 nm for each dimension. To eliminate the presence of water vapor, the sample was kept for several hours in an oven at a constant temperature of 150 °C.

The sample is placed on the plane surface of a prism, and the optical matching is achieved by an index matching liquid. Our experimental setup (Fig. 1) is a PSTM,[2] in which the probe locally detects the electromagnetic field around the sample. The PSTM exploits the tunneling of photons across the gap between the sample illuminated by a He-Ne laser ($\lambda = 632.8$ nm, $P = 2.8$ mW) in a TIR configuration, to eliminate a great part of the propagative waves. A sharpened optical fiber probe is brought into the scattered evanescent field and collects a part of this evanescent field. The propagative waves scattered by the sample are also detected by the fiber tip. When the probe is scanning parallel to the surface, this is the so-called ''constant height'' mode. Practically it is not possible to be sure that the probe apex remains strictly at a constant distance above the mean surface of the sample, especially when large ranges are scanned. The mechanical and thermal drifts perturb the experiment in the same way. Thus this constant height mode is very difficult to use. Another mode of operation is the ''constant intensity'' mode, in which the intensity recorded by the probe is kept constant, using an electronic feedback driving a piezoelectric scanner unit on which the probe is fixed. This mode is the most commonly used, but the corresponding calculations are more difficult to implement than for the constant height mode. This mode can also be used to obtain a reference surface. If we simultaneously detect the scattered light issued from a second source while the probe is scanning a reference surface we are operating in the two-wavelength mode. Before giving the experimental results, we describe our way to compute the scattered field above the metallic pads.

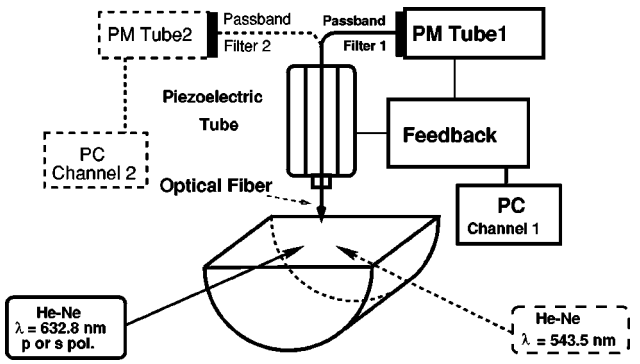

FIG. 1. Schematic of the experimental setup of the two-wavelength mode. The constant intensity mode is represented in solid lines.

III. ANALYSIS OF THE ELECTROMAGNETIC FIELD ABOVE THE SAMPLE

To analyze the electromagnetic field diffracted by a crossed grating of parallelepipedic pads and collected by the optical fiber of the previous experimental setup, here we present the theoretical approach used to obtain the near-field intensity of the electromagnetic field produced by a crossed Au grating laid on a glass prism and illuminated in TIR. We use the differential formalism of the electromagnetic theory of gratings.[13] The exact geometry of the crossed grating has been chosen according to the scanning electron microscopy images obtained after metallization on a test sample. Each pad is parallelepipedic, with lateral dimensions $s_x = s_y = 300$ nm and height h$=$ 50 nm (Fig. 2). The groove spacing in the x and y directions is $d_x = d_y = 3$ μm (Fig. 3). The incident plane wave with unit amplitude, and a wavelength $\lambda_0 = 2\pi/k_0$ in vacuum, falls on the crossed grating under the angles of incidence determined by θ_k ($\mathbf{k}_{inc}$, $\mathbf{e}_z$) and φ_k ($\mathbf{e}_x$, $\mathbf{k}_{//}$) defined in Fig. 3. For the calculations, the space is divided into three zones (zone 1 for $z > h$, a modulated zone for $h > z > 0$, and zone 2 for $z < 0$; see Fig. 2). In this paper, the sample is illuminated through the prism side (zone 1), where the index of refraction n_1 is equal to 1.458. The incident electric field $\mathbf{E}$, in s polarization, is parallel to the x axis, $\mathbf{E}_x(x,y,z) = \mathrm{E}_x(x,y,z)\ \mathbf{e}_x$ ($\mathbf{e}_x$ is the unit vector of the Ox axis). The electric and magnetic fields above the crossed grating are expanded as double sums over Rayleigh waves.

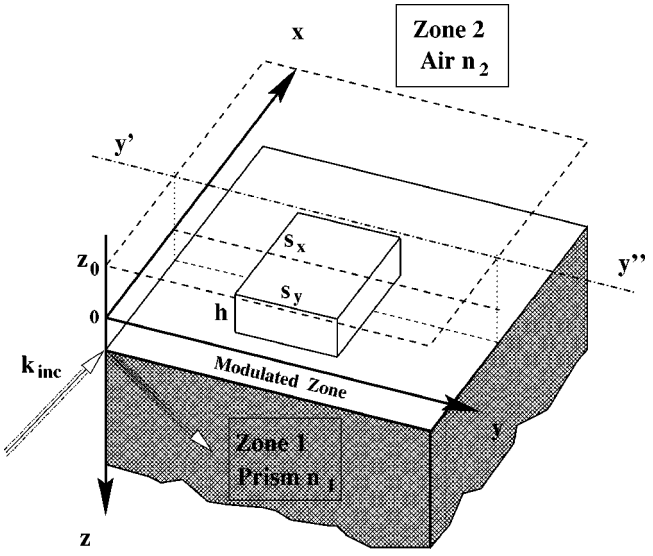

FIG. 2. Geometry of the pad. The height of the metallic pad is $h=50$ nm, and the size of its square section is $s_x=s_y=300$ nm. The optical index of the prism is equal to 1.458, and the parallelepiped's optical index is equal to $n_{Au}=0.149+j3.64$ for the incident wavelength equal to 632.8 nm. $z=z_0$ defines the observation plane, and $(y'y'')$ the crosscut line.

In particular, for s polarization, the electric field in the zone 2 (air side with $n_2=1.0$) below the crossed grating can be written as[13]

$$\mathbf{E}(x,y,z)=\sum_{n=-\infty}^{+\infty}\sum_{m=-\infty}^{+\infty}\mathbf{A}_{n,m}^{E}\exp[j(\alpha_n x+\beta_m y)]\exp(-j\gamma_{n,m}z) \tag{1}$$

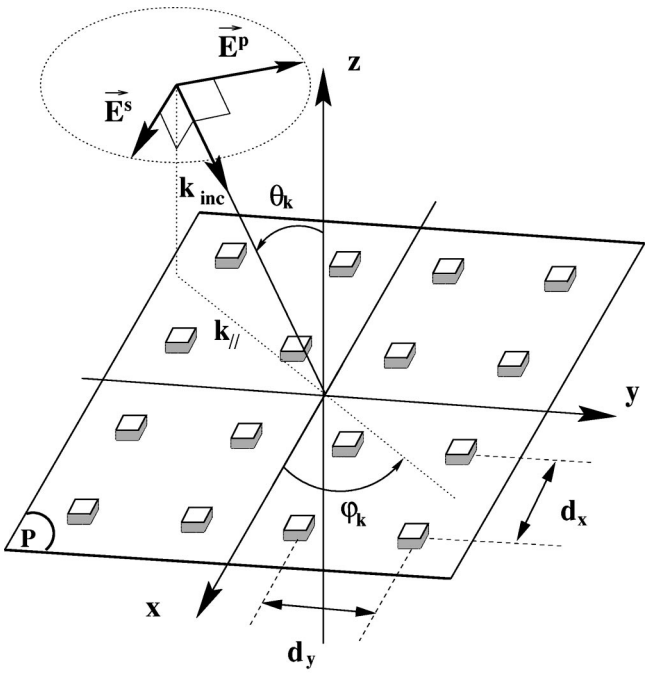

FIG. 3. Crossed grating of metallic pads. The system is illuminated in total internal reflection, and $\mathbf{k_{inc}}$ represents the wave vector associated with the incident wave. $\mathbf{k}_{//}$ is the projection of this incident wave vector on the plane (P). $d_x=d_y=3$ μm.

when $z<0$, with

$$\alpha_n=\alpha_0+n2\pi/d_x,\quad \alpha_0=k_0 n_1\sin\theta_k\cos\varphi_k,$$

$$\beta_m=\beta_0+m2\pi/d_y,\quad \beta_0=k_0 n_1\sin\theta_k\sin\varphi_k,$$

and

$$\gamma_{n,m}=\sqrt{k_0^2n_2^2-\alpha_n^2-\beta_m^2}\quad\text{if}\quad k_0^2n_2^2\geqslant\alpha_n^2+\beta_m^2\quad\text{(radiative modes)}$$

$$=j\sqrt{\alpha_n^2+\beta_m^2-k_0^2n_2^2}\quad\text{if}\quad k_0^2n_2^2\leqslant\alpha_n^2-\beta_m^2\quad\text{(evanescent modes)}.$$

The unknown functions of the problem are the complex amplitudes $\mathbf{A}_{n,m}^{E}$ for the electric field. It is possible to write the magnetic field by an expression similar to Eq. (1). In this case the complex amplitudes will be noted $\mathbf{A}_{n,m}^{H}$. As in the case of the two-dimensional (2D) differential method, the main idea to solve this problem is to find for both $\mathbf{E}(x,y,z)$ and $\mathbf{H}(x,y,z)$, propagation equations valid in the whole space in the sense of distributions, which includes the boundary conditions at the two boundaries of the modulated zone. As for a 1D grating, we take the two equations of Maxwell and Faraday and Maxwell and Amphre. From these two vectorial equations (i.e. the six scalar corresponding equations), it is possible to eliminate the components along the z axis to obtain ultimately a system of four partial differential equations depending on the four remaining components E_x, E_y, H_x, and H_y. These equations are true in the sense of the functions as well as in the sense of the distributions. They are written as

$$\frac{\partial E_x}{\partial z}=j\omega\mu_0 H_y+\frac{\partial}{\partial x}\left[\frac{-1}{j\omega\epsilon_0\epsilon_r}\left(\frac{\partial H_y}{\partial x}-\frac{\partial H_x}{\partial y}\right)\right], \tag{2}$$

$$\frac{\partial E_y}{\partial z}=-j\omega\mu_0 H_x+\frac{\partial}{\partial y}\left[\frac{-1}{j\omega\epsilon_0\epsilon_r}\left(\frac{\partial H_y}{\partial x}-\frac{\partial H_x}{\partial y}\right)\right], \tag{3}$$

$$\frac{\partial H_x}{\partial z}=-j\omega\epsilon_0\epsilon_r E_y+\frac{\partial}{\partial x}\left[\frac{1}{j\omega\mu_0}\left(\frac{\partial E_y}{\partial x}-\frac{\partial E_x}{\partial y}\right)\right], \tag{4}$$

$$\frac{\partial H_y}{\partial z}=j\omega\epsilon_0\epsilon_r E_x+\frac{\partial}{\partial y}\left[\frac{1}{j\omega\mu_0}\left(\frac{\partial E_y}{\partial x}-\frac{\partial E_x}{\partial y}\right)\right], \tag{5}$$

where $\epsilon_r=\epsilon_r(x,y,z)=n_i^{\,2}(x,y,z)$ according to the values of x, y, and z in the different zones (zones 1 and 2 and the modulated zone).

Details of the differential method were given elsewhere.[14,15] These partial differential equations (2)–(5) are then transformed into a finite set of coupled differential equations by Fourier analysis. The integration of the differential system is reduced to the interval $[0,h]$ along z, due to the existence of analytical solutions for the field outside the modulation region [see Eq. (1) for $z<0$]. Inside the modulated region, the integration is made numerically by a Runge-Kutta algorithm. By writing the boundary conditions for the electric and magnetic fields at $z=0$ and $z=h$ and by using the standard matrix inversion techniques, we calculate the amplitudes $(A_x)_{n,m}^{E}$, $(A_y)_{n,m}^{E}$ and $(A_x)_{n,m}^{H}$, $(A_y)_{n,m}^{H}$ of the

electric and magnetic fields. Once these amplitudes are known, the two remaining amplitudes $(A_z)^E_{n,m}$, and $(A_z)^H_{n,m}$ are obtained from the two following equations:

$$E_z = \frac{j}{\omega \epsilon_0 \epsilon_r}\left(\frac{\partial H_y}{\partial x} - \frac{\partial H_x}{\partial y}\right), \tag{6}$$

$$H_z = \frac{1}{j\omega\mu_0}\left(\frac{\partial E_y}{\partial x} - \frac{\partial E_x}{\partial y}\right). \tag{7}$$

Then, the electric field **E** can be calculated with the expression of expansion (1) at any point around the crossed grating, close to the metallic pad. The magnetic field **H** is similarly obtained. The field is accurately represented by N^2 components, and this number is chosen according to the stability of the numerical results.

To illustrate the possibilities of this technique, we now give different remarks about the electromagnetic field calculated above the crossed grating in the constant height mode. The plane of incidence is defined by the two vectors $\mathbf{k}_i$, $\mathbf{e}_z$, and $\mathbf{k}_{//}$ is the projection of $\mathbf{k}_i$ on the (Oxy) plane (see Fig. 3). In our case of diffraction, the two angles are $\theta_k = -60°$ and $\varphi_k = 90°$. The square modulus of the electric field is calculated for Au pads whose index of refraction is equal to $n_{Au} = 0.149 + j3.64$, for a wavelength in vaccum equal to 632.8 nm. According to the conditions of preparation of the sample, we suppose that the experimental values of the permittivity of Au pads are close to those given by Johnson and Christy.[18].

In Figs. 4(a) and 4(b), we plot the theoretical variations of the intensity normalized to the incident intensity I_0 ($I_0 = |E_0|^2$) over a period of the crossed grating in constant height mode in planes located at, $z_0 = -60$ and -150 nm above the top of the pad, respectively. We have chosen these z_0 values because they correspond to classical probe-to-sample distances in PSTM experiments. The profiles, along the axis $(y'y'')$ ($x = d_x/2$, $z = z_0$, Fig. 2); are reported in Fig. 4(c). The simulations of the field diffracted by the pads are presented in s polarization. Figure 4 shows a strong intensity diffracted close to the metallic pad. We note that the maximum intensity above the pad is three times greater than that above the substrate. We also see that the electromagnetic field pattern is strongly modified as a function of the distance from the Au pad. A full study of the field as a function of the distance from the sample shows that, for $|z_0| < 100$ nm, the effects of the edges are well pronounced, as we see in Fig. 4(a). This study also demonstrates that the electromagnetic field remains confined for a probe-to-sample distance less than λ, with a relative enhancement (ratio of the maximum intensity diffracted by the pads and the intensity in the near-field of the substrate) varying between 3 and 10. In Fig. 4, we show a complicated standing-wave pattern[10,19] which is also observed experimentally in Sec. IV. This interference pattern is due to the interaction of the resulting diffracted surface waves provided by the pads on the substrate.

As shown previously for a dielectric crossed grating,[19] the amplitude of the field depends strongly on the probe-to-sample distance, and also on the polarization. The *s* polarization is reported in Fig. 4, while Fig. 5 shows the *p* polarization for the same two distances $z_0 = -60$ and -150 nm. For the two different polarizations we expect that the diffraction

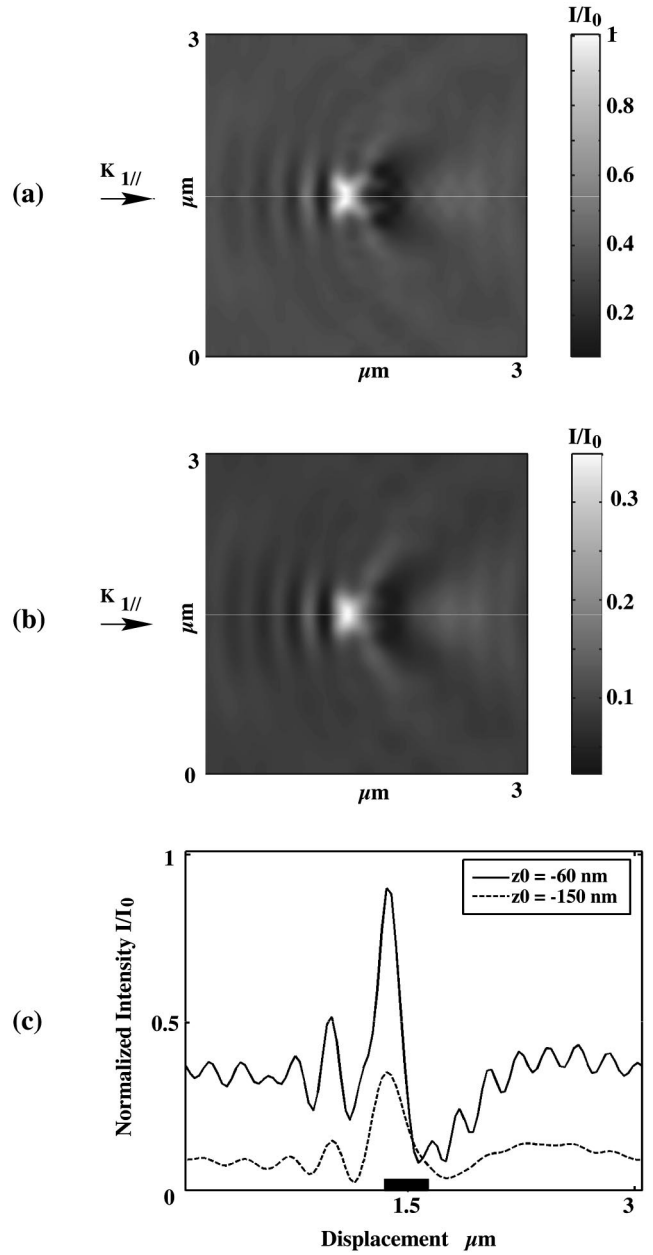

FIG. 4. Top view of a 3D image of the normalized intensity, $I/I_0 = |\mathbf{E}|^2/|\mathbf{E}_0|^2$ calculated above the crossed grating given in Fig. 2. The calculation is made in *s* polarization ($\lambda_0 = 632.8$ nm, $\theta_k = -60°$, and $\varphi_k = 90°$). The value of the normalized intensity I/I_0 is calculated in a plane defined by $z_0 = -60$ nm in (a) and $z_0 = -150$ nm in (b). In (c), we represent the normalized intensity according to the axis $(y'y'')$ (Fig. 2) in *s* polarization for the two altitudes.

of the pad edges will be different, as the edge is parallel or perpendicular to $\mathbf{E}_{inc}$. Figures 4 and 5 show that the field distributions are really different. We observe strong localizations of the field, whose characteristics depend strongly on the polarization. It is important to note that these localizations can be of smaller size surface than the pad itself [see the profiles in Figs. 4(c) and 5(c)].

The intensity distribution around the pads depends on their shape and their repeat distance, but also on their index of refraction. Here we compare the electromagnetic field scattered by metallic pads to the electromagnetic field scat-

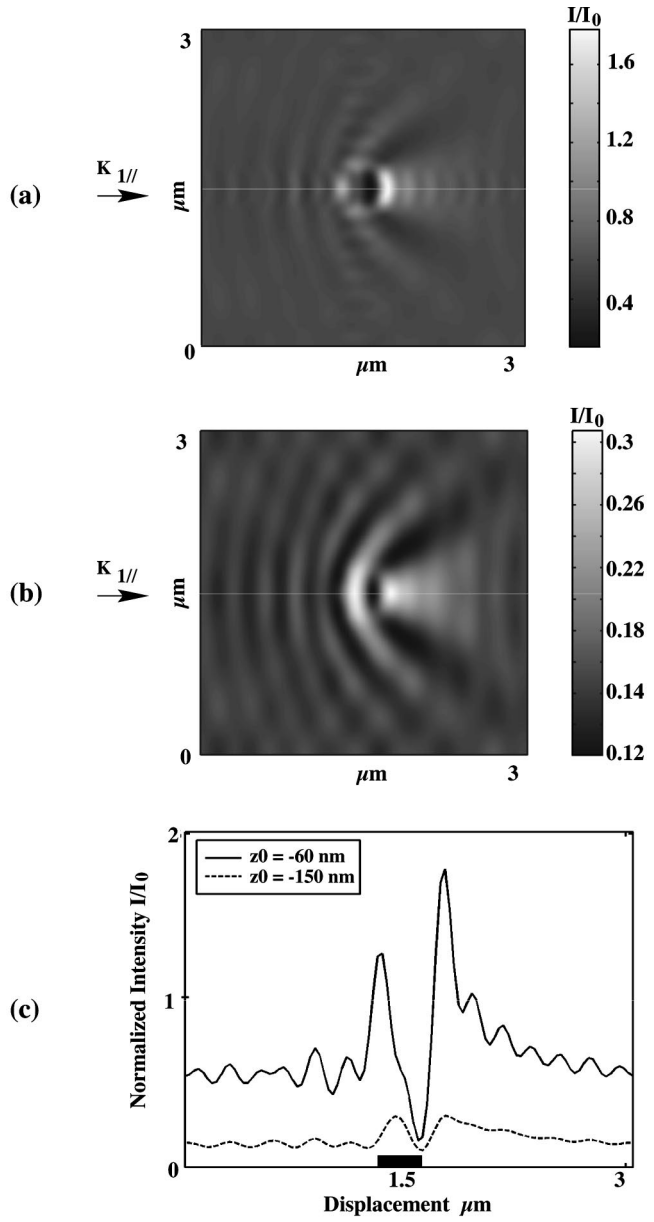

FIG. 5. Top view of a 3D image of the normalized intensity, $I/I_0=|\mathbf{E}|^2/|\mathbf{E}_0|^2$, calculated above the crossed grating given in Fig. 2. The calculation is made in p polarization ($\lambda_0=632.8$ nm, $\theta_k=-60°$, and $\varphi_k=90°$). The value of the normalized intensity I/I_0 is calculated in a plane defined by $z_0=-60$ nm in (a) and $z_0=-150$ nm in (b). In (c), we represent the normalized intensity according to the axis ($y'y''$) in p polarization for the two altitudes.

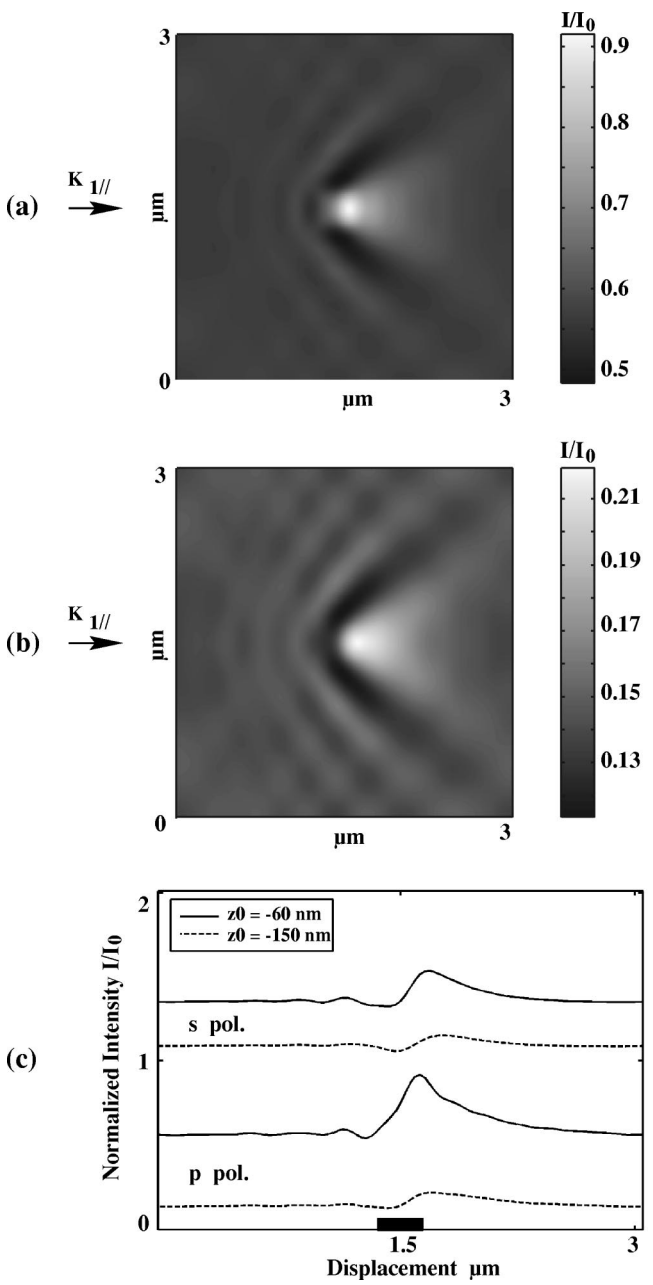

FIG. 6. Top view of a 3D image of the normalized intensity, $I/I_0=|\mathbf{E}|^2/|\mathbf{E}_0|^2$, calculated above the crossed grating formed by dielectric pads in the same configuration as in Fig. 2. The calculation is made in p polarization ($\lambda_0=632.8$ nm, $\theta_k=-60°$, and $\varphi_k=90°$), (a) is obtained for $z_0=-60$ nm, and (b) for $z_0=-150$ nm. In (c), we represent the intensity along the axis ($y'y''$). We have also represented the cross sections for the two polarizations and for the two distances: $z_0=-60$ nm and $z_0=-150$ nm. For the sake of clarification, the intensities are shifted upwards by 1 for the two cross sections in s polarization.

tered when the pads and the substrate are of the same nature. When investigating near-field diffraction effects, it is important to consider the dielectric contrast between the pads and their environment. For the same illumination parameters, we in Fig. 6 represent the intensity scattered by dielectric pads illuminated in p polarization [$n_{diel}=n_1=1.458$ and $d_x=d_y=3$ μm, in Fig. 6(a), and $z_0=-60$ and -150 nm in Fig. 6(b)]. The geometry of the sample is identical to the geometry of the sample with the metallic pads. Figure 6(c) shows the profiles along $y'y''$ for the two polarizations and for the two distances: $z_0=-60$ and -150 nm. From the figures, one observes that for a given polarization of the incident light and for the same altitude z_0, the intensity of the electric field reaches greater values near metallic pads than near dielectric pads. This is due to the dielectric constrast between the pads and their environment (the media around the pads). For dielectric pads, the maximum of the intensity is greater in p polarization than in s polarization at a given distance from the sample [see Fig. 6(c)]. For the metallic pads, beyond a definite distance (about 130 nm for $300\times300\times50$-nm^3 Au pads, and $d_x=d_y=3$ μm), the maximum of the intensity is

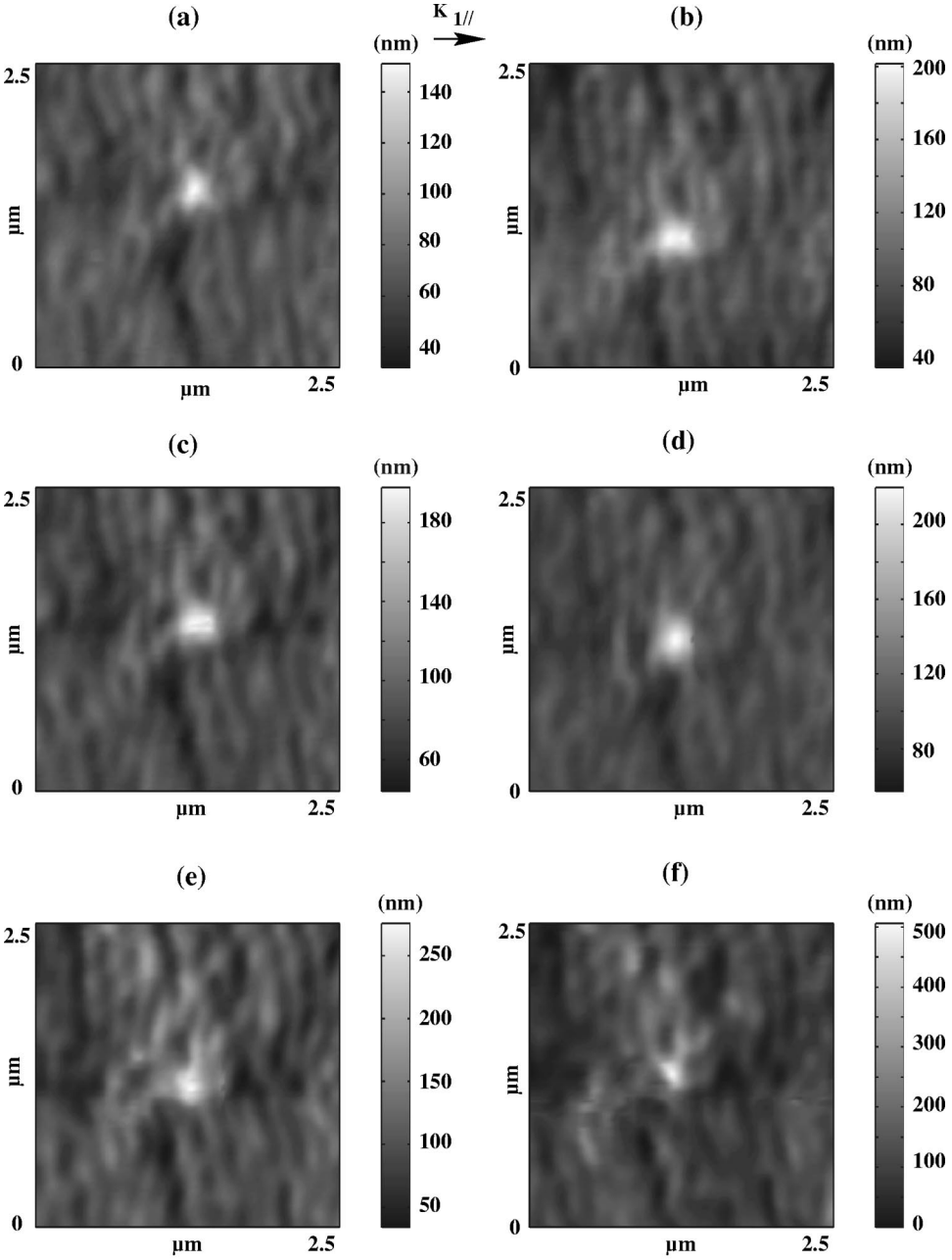

FIG. 7. Experimental PSTM images obtained in the constant intensity mode for $\theta_k = -60°$, and $\varphi_k = 90°$ in *s* polarization, with $\lambda_0 = 632.8$ nm. The lateral and vertical dimensions of the Au pads are $300 \times 300\ \mathrm{nm}^3$ and 50 nm. The sequence of images in the top part of a 3D view describes the evolution of the electric field for different probe-to-sample distances. The different images (a)–(f) are obtained for $|z_0| = 45$ nm, $|z_0| = 100$ nm, $|z_0| = 140$ nm, $|z_0| = 180$ nm, $|z_0| = 280$ nm and $|z_0| = 350$ nm, respectively; these values are given for the center points of the images.

greater in *s* polarization than in *p* polarization [compare the profiles Figs. 4(c) and 5(c)]. This behavior is very different from that of a continuous thin metallic film.[2] In this case, the intensity near the metal-air interface is always greater in *p* polarization than in *s* polarization. By looking more finely at our results, we note that the intensity in the center of the pad is higher in *p* polarization than in *s* polarization, and that the oscillations around the pads are weaker around the dielectric pads than the metallic pads. We also see that the oscillation amplitudes near the metallic pad decrease when the distance vertically increases. This is an indication that these oscillations are issued from the reflections of the evanescent components which propagate on the substrate-air interface, and together interfere.

Experimentally, it is difficult to obtain images in the constant height mode. That is the reason why the constant intensity mode is widely used in near-field microscopies. Although Carminati and Greffet[20] showed analytically that the constant intensity image is qualitatively ''proportional'' to the constant height image for a dielectric or metallic mesoscopic structure, we have chosen to compare quantitatively our experimental and simulated images obtained in the constant intensity mode. This comparison is presented in the next Sec. IV.

IV. IMAGES OBTAINED IN THE CONSTANT INTENSITY MODE

Due to the previously mentioned difficulties in the constant height mode, we choose to study our sample in the constant intensity mode. During our experiments, we have recorded a set of images in *s* (Fig. 7) and *p* (Fig. 8) polarizations for different intensity setpoint values. To compare the experimental images with our simulated images, we determine for each of them the distance between the probe and the surface for the center of the scanning range. We can

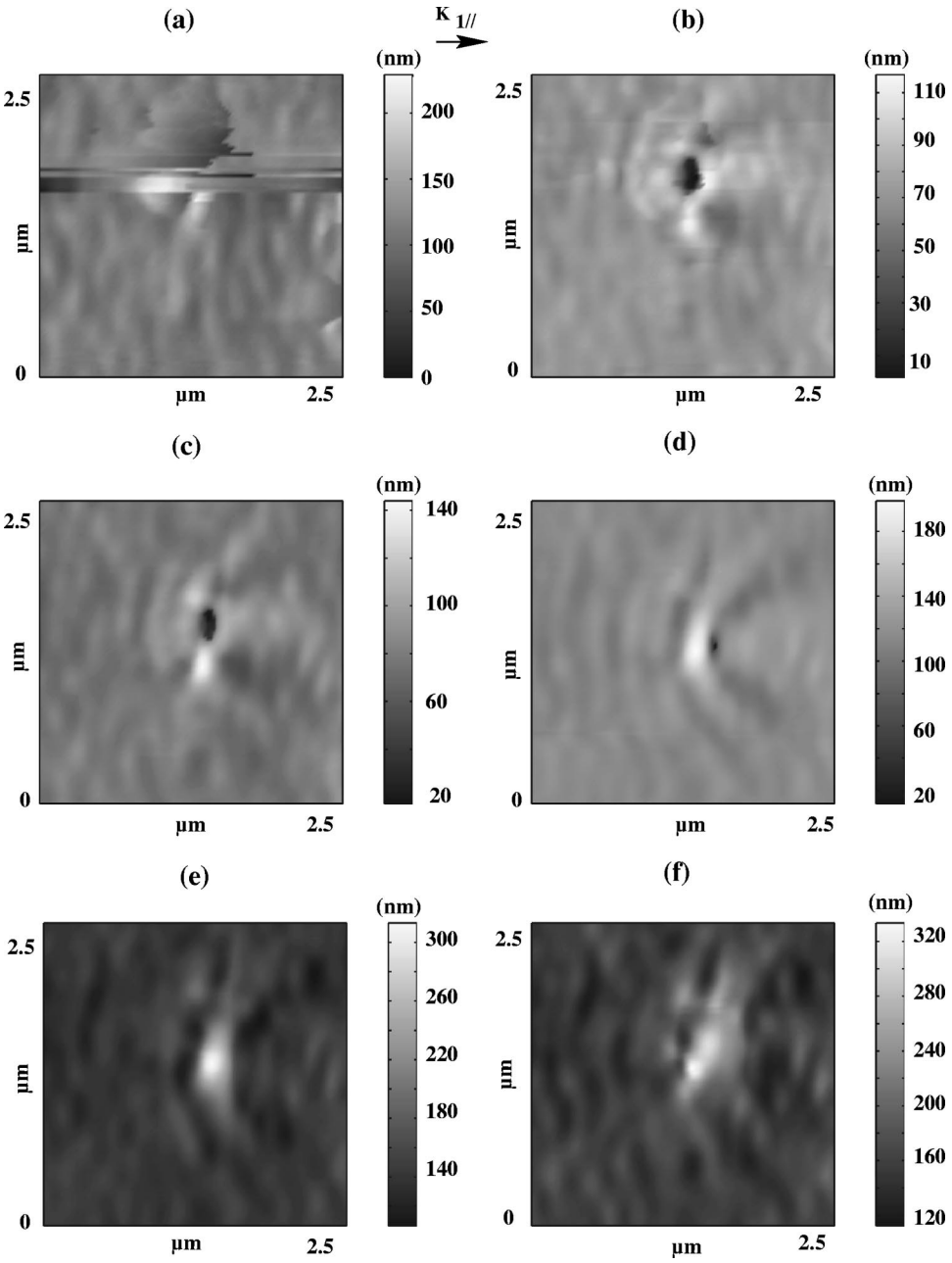

FIG. 8. The same sequence of PSTM images as in Fig. 7, but obtained in *p* polarization. The different images (a)–(f) are obtained for $|z_0|=0$ nm, $|z_0|=40$ nm, $|z_0|=80$ nm, $|z_0|=130$ nm, $|z_0|=220$ nm, and $|z_0|=370$ nm, respectively; these values are given for the center points of the images.

determine the exact distance of the probe in the center for each image because, on the last image [Fig. 8(a)], the probe has touched the top of the pad, and as we changed the value of the setpoint of a well-defined value between two consecutive images, we obtained a variation of the vertical probe position between these two images.

The sample studied here is described in Sec. II. We have repeated the experiments in *s* polarization then in *p* polarization, with the following parameters: $\lambda=632.8$ nm, $\theta_k=-60°$, and $\varphi_k=90°$. We have systematically studied the isointensity images of the electromagnetic field scattered by the sample on a 2.5×2.5-μm^2 scanning range for different intensities. On the two sets of images obtained in *s* and *p* polarizations, respectively, the probe moved away in the order of 350 nm. The images presented in Figs. 7(a)–7(f) are recorded for fiber-to-sample distances (in the center of the image) equal to $|z_0|=45$, 100, 140, 180, 280, and 350 nm, respectively, in *s* polarization. In *p* polarization, the six images shown in Fig. 8(a)–8(f) have been recorded for distances equal to $|z_0|=0$, 40, 80, 130, 220, and 370 nm, respectively.

The intensity above the metallic pad is described by a Rayleigh expansion, so it is relatively easy to reconstruct the images in the constant intensity mode. The knowledge of the absolute distances allows us to simulate the different images (Figs. 9 and 10) obtained in the constant intensity mode, corresponding to the experimental images. In this mode we represent the displacement (in nanometers) of the probe with an absolute error in *z* equal to 1 nm. In *s* and *p* polarizations, the images presented have been calculated with the values determined from the experimental recordings.

We notice an excellent agreement between the experimental and simulated images, especially in *p* polarization. The set of images in *s* and *p* polarizations recorded versus probe-sample distance [except in Figs. 7(a), 8(f), 9(f), and 10(f), where we leave the near-field zone] shows very differ-

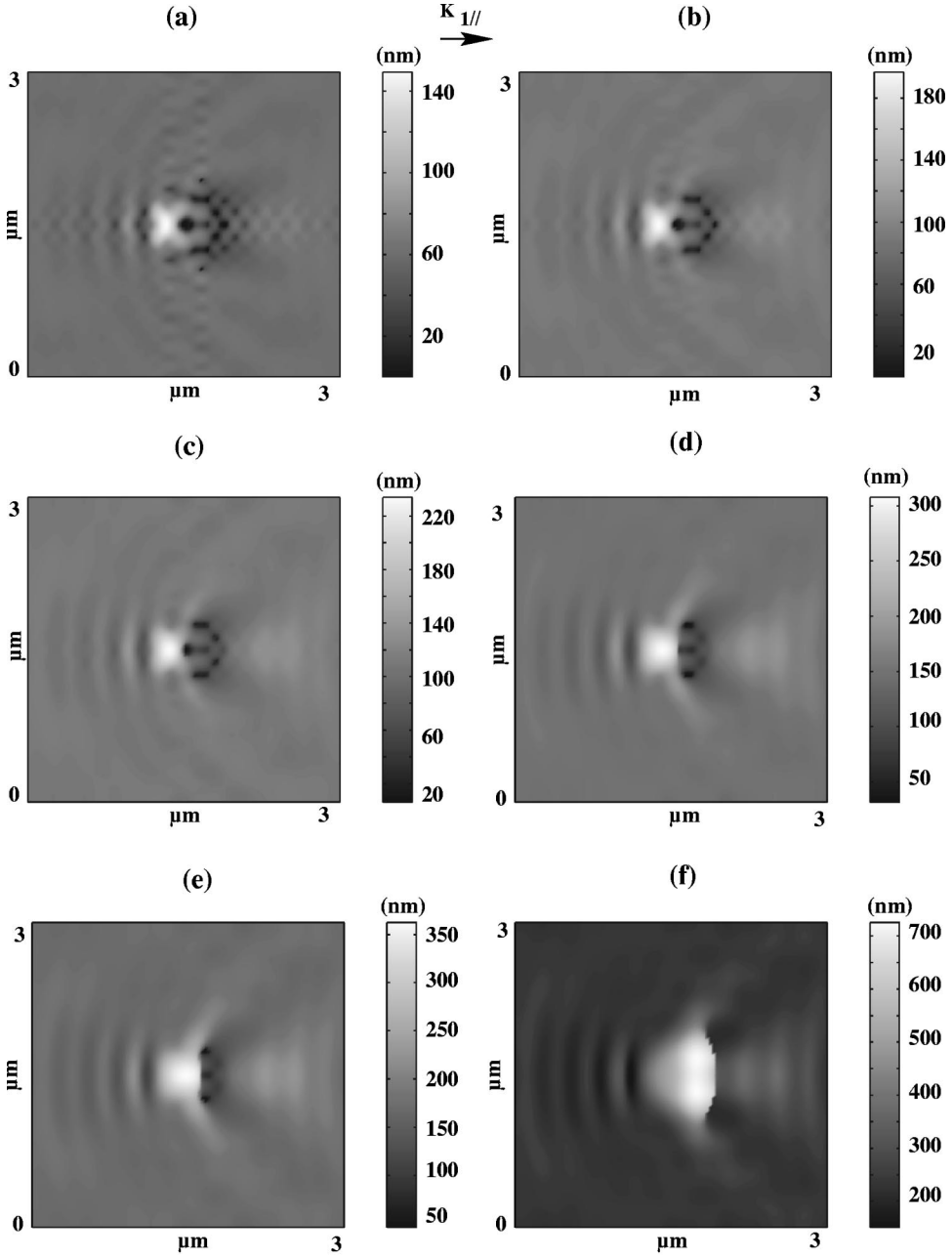

FIG. 9. Calculated images obtained with the differential method, $\lambda_0 = 632.8$ nm, $\theta_k = -60°$, and $\varphi_k = 90°$, in the constant intensity mode, in *s* polarization. The sequence of images from (a) to (f) is obtained for intensities equal to $I/I_0 = 0.35$, $I/I_0 = 0.26$, $I/I_0 = 0.23$, $I/I_0 = 0.166$, $I/I_0 = 0.093$, $I/I_0 = 0.066$, and $I/I_0 = 0.025$, respectively.

ent forms, and have various evolutions versus probe-sample distance. In *s* polarization the field is always confined near the pads, and its distribution evolves slowly versus probe-sample distance in experimental and computed images. In *p* polarization the field distribution takes particular and complicated shapes. The field distribution evolves clearly versus distance: it makes it easy to compare theoretical and experimental results. On the two sets of recorded images, the electromagnetic field around the metallic pads appears more confined laterally in *s* polarization than in *p* polarization (Figs. 7 and 8). In *p* polarization, we see that the electromagnetic intensity above the Au pads appears as a pattern of diffraction with a lobe in crescent shape [Figs. 8(b)–8(d)]. This lobe disappears as the fiber leaves the evanescent region [Figs. 8(e) and 8(f)]. In Figs. 8(a)–8(d) and 10(a)–10(d), we note the presence of a marked and localized hole above the metallic pad. Some oscillations appear around the pad: they are more visible in the theoretical images [Figs. 10(b)–10(f)]. We obtain such oscillations principally in *p* polarization [Figs. 8(c)–8(e)]. It is important to remark that the two sets of images (Figs. 7 and 9) show a significant spatial localization. However (principally in *s* polarization; see Fig. 7), the oscillations and localizations due to the interferences of the surface waves are partly hidden and attenuated by the ''speckle structure'' resulting from the illumination of the sample by a coherent source.[21] This is particularly true for great probe-to-sample distances, as shown in two sets of figures: Figs. 7(f) and 9(f), and 8(f) and 10(f). This phenomenon is more marked for important probe-to-sample distances. We note that the agreement between experimental data and simulations is quantitative in *s* and in *p* polarizations. This is shown by the vertical bars (on the right of the images) representing the correspondence between the gray scales and the displacements of the tip. However, Fig. 8(a) strongly differs from the calculated image [Fig. 10(a)]. This difference can be explained by the two following hypoth-

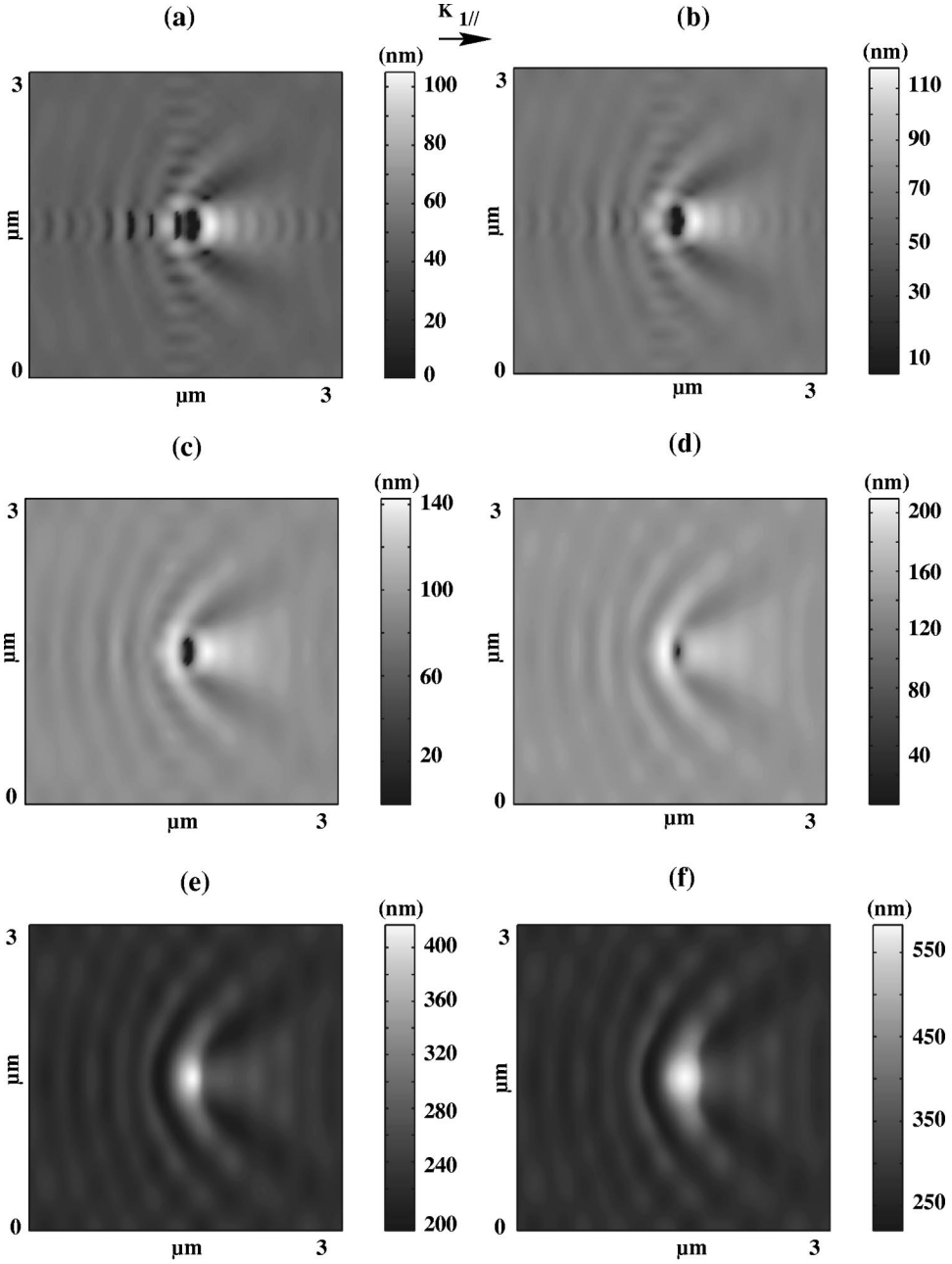

FIG. 10. The same sequence of calculated images as in Fig. 9 in *p* polarization. The sequence from (a) to (f) is obtained for intensities equal to $I/I_0=0.7$, $I/I_0=0.55$, $I/I_0=0.35$, $I/I_0=0.165$, $I/I_0=0.045$, and $I/I_0=0.02$, respectively.

eses: first, during the scanning of Fig. 8(a) the tip touched the pad surface; and, second, for short sample-to-probe distances the assumption of a passive probe is not valid. From the whole serie of images obtained in the near-field of the metallic pads this assumption appears to be valid for distances higher than a few tens of nanometers. In this case, as previously demonstrated for dielectric samples and probes,[16,17] the intensity recorded is proportional to the square modulus $|\mathbf{E}|^2$ of the electric field in the absence of the probe. For shorter distances, a simulation taking into account the probe will allow us to describe more exactly the collected intensity above the pad.

V. IMAGES OBTAINED IN THE TWO-WAVELENGTH MODE

Through the agreement between experiments and simulation is good, one needs to record a great number of images to be able to compare quantitatively results obtained with *s* or *p* polarized incident light. Indeed, in the constant intensity mode previously described, two independent images obtained in *s* and *p* polarizations cannot be directly compared, as the paths followed by the tip during the two scannings are not the same. Therefore we thought of another experimental method, described below. We performed measurements with two illuminating sources at different wavelengths (Fig. 1). The first beam, a He-Ne laser, at wavelength $\lambda_{ref}=534.5$ nm (reference wavelength) is unpolarized ($P=1$ mW), while the second beam from a He-Ne laser at wavelength $\lambda_2=632.8$ nm is *s* or *p* polarized. These two different laser beams have symmetric angles of incidence ($\theta_{k1}=-60°$, $\varphi_{k1}=90°$ and $\theta_{k2}=60°$, $\varphi_{k2}=-90°$; see Fig. 1). While the optical fiber tip is scanning, the collected light is divided into two parts by a 2×2 fiber coupler with a power coupling efficiency of 50%. Light coupled into the right arm of the coupler is filtered to suppress the λ_2 wavelength. The remaining light, at the ref-

erence wavelength λ_{ref}, enables one to control the vertical motion of the tip. We obtain an image in the constant intensity mode which defines a reference surface to be used subsenquently. Light coupled into the left arm of the coupler is filtered to suppress the λ_{ref} wavelength, and is recorded by a photomultiplier tube to form another image at λ_2.

Thus we perform several consecutive scannings above the same surface of the sample, changing only the polarization of the second beam. The images obtained in these two polarizations at $\lambda_2 = 632.8$ nm (with reference at $\lambda_{ref} = 543.5$ nm) can directly be compared. Such a comparison is relevant provided that the probe does not touch the sample or the feedback system does not fail to follow the same isointensity surface at λ_{ref} when the λ_2 beam is changing from *s* to *p* polarization.

Figure 11(a) is an image taken at $\lambda_{ref} = 543.5$ nm in the constant intensity mode, and Fig. 11(b) shows an image taken simultaneously at $\lambda_2 = 632.8$ nm in *s* polarization. The image corresponding to *p* polarization, taken in a similar manner, is shown in Fig. 11(c). We do not represent the constant intensity image recorded simultaneously with Fig 11(c): it is identical to Fig. 11(a). In the images, only nine pads appear because the scanning range reaches the edge of the grating. In Fig. 11, the nine pads are not similar, and therefore their electromagnetic diffraction patterns are different. This is probably due to the position of these pads on the edge of the grating, and also perhaps to a damaging of the sample. In spite of this, the near-field of metallic pads is well distinguished on the images, despite the presence of polluting agents (dust particles), and the fact that the speckle structure hide the oscillations around the metallic pads. In Figs. 11(b) and 11(c), we observe a polarization-dependent behavior when the fiber probe follows the reference surface. Before discussing experimental and theoretical results in this two-wavelength mode, we observe, from the gray scales on the right of Figs. 11(b) and 11(c), that the detected intensity is stronger in *s* polarization, as it was already emphasized in the constant intensity mode.

In Fig. 12, we represent the same sequence of images simulated with the differential method. The calculated image at the reference wavelength [Fig. 12(a)] is obtained for a crossed grating with Au pads. To simulate the sample illumination with an unpolarized laser beam at $\lambda_{ref} = 543.5$ nm, we averaged the intensities obtained for *s* and *p* polarizations, respectively. The two images computed in Figs. 12(b) and 12(c), respectively, calculated with the wavelength $\lambda_2 = 632.8$ nm in *s* and *p* polarizations, are obtained from Fig. 12(a) with a normalized constant intensity equal to 0.35. The reference surface corresponding to the image obtained at $\lambda_{ref} = 543.5$ nm shows that the distance to the sample is always greater than 140 *nm* above the pads. Under these conditions, the maximum intensity recorded in *s* polarization is greater than in *p* polarization. This result is in agreement with the result given in Secs. III and IV. Although the images are complicated, we find quite a good agreement between theory and experiment. This is true for the localizations of the optical intensity above and near the pads, as well as for the intensity modulations between the pads [Figs. 11(c) and 12(c)]. We see clearly in Figs. 12(b) and 12(c), and slightly on Figs. 11(b) and 11(c), a symmetrical pattern between the pads due at left to the reference surface and at right

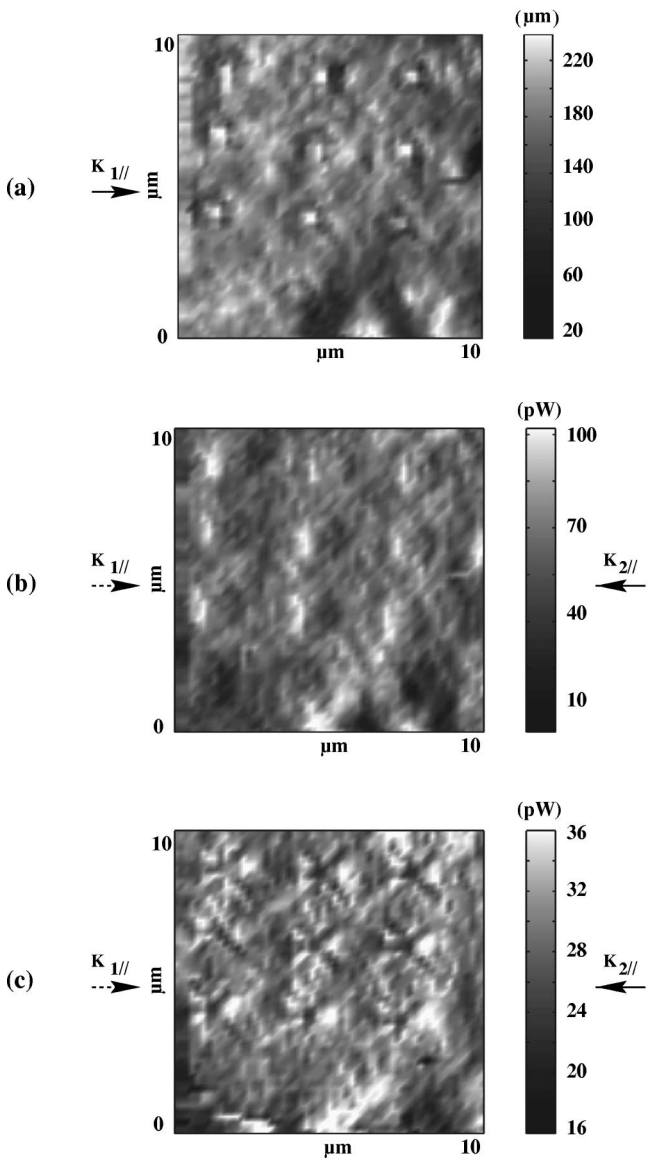

FIG. 11. Experimental PSTM images obtained in the two-wavelength mode. The lateral and vertical dimensions of the metallic pads are 300×300 nm^2 and 50 nm). (a) is a top view of a 3D image of the displacement of the optical fiber probe in nanometers, obtained in the constant intensity mode. The reference wavelength $\lambda_{ref} = 543.5$ nm is obtained with the unpolarized He-Ne laser. (b) and (c) are top views of 3D images of the intensity collected (in pW) for $\lambda_2 = 632.8$ nm in *s* and *p* polarizations, respectively. (b) and (c) are recorded simultaneously with images obtained in the constant intensity mode (a). The conditions of illumination with the two wavelengths are symmetrical, as indicated in Fig. 1: $\theta_{k1} = -60°$, $\varphi_{k1} = 90°$, $\theta_{k2} = 60°$, and $\varphi_{k2} = -90°$.

to the $\lambda = 632.8$ nm source. In Fig. 11(b), we note an exaltation of the localized electromagnetic field along a line perpendicular to the projection on the substrate-air interface of the wave vector $\mathbf{k}_2$. This increase of the intensity is apparent on a band of width about 100 nm. The corresponding theoretical scattered intensity [Fig. 12(b)] shows a structure with the same size. However, Fig. 12(c) shows an increase of the intensity of light at each extremity of these lines, which is not obvious on the experimental images. This should be attributed to the integration of the electromagnetic field by the

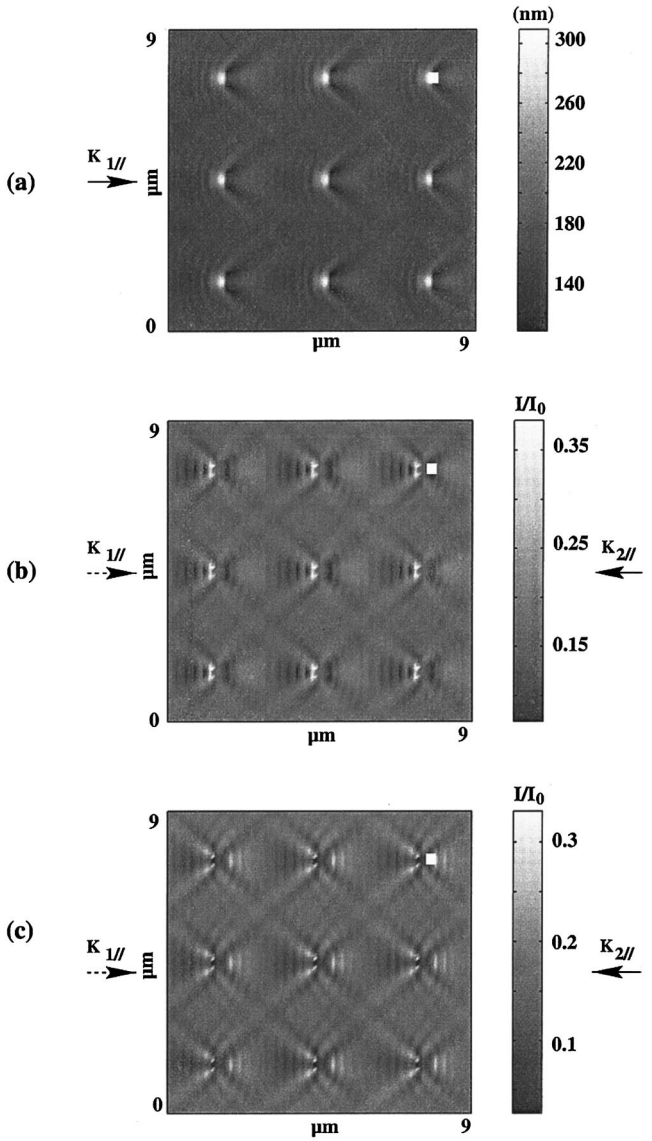

FIG. 12. Calculated images obtained in the two-wavelength mode. (a) is a top image of a 3D image representing the displacement of the probe obtained in the constant intensity mode. The unpolarized reference wavelength, $\lambda_{ref}=543.5$ nm ($n_{Au}=0.376+j2.613$), is obtained from a mixed intensity: 50% in *s* polarization and 50% in *p* polarization. The lateral and vertical dimensions of the metallic pads are the same as in Fig. 11. (b) and (c) are top views of 3D images of the normalized intensity for $\lambda_2=632.8$ nm in *s* and *p* polarizations, respectively. For the simulation, we have respected the same conditions of illumination as for the recording of the experimental images (Fig. 11). We have represented one of the Au pads on each image at the top right corner.

probe whose size is about 100 nm.

These results demonstrate that with the two-wavelength mode, it is possible to separate the effect of polarization from the effect of the probe-to-sample distance (see the hasty conclusions given in Ref. 5 to separate the effects of polarization and wavelength). This mode could be used to discriminate the effect of other parameters such as the wavelength (λ_2) or the angle of incidence (θ_2) to observe, for example, a local enhancement of the field for a fixed reference beam. In addition, this two-wavelength mode, by the choice of the reference wavelength (λ_{ref}) and the angle of incidence (θ_{ref}), allows one to vary continuously the distance of operation in the evanescent zone, and consequently to choose a suitable reference surface for a study of a particular phenomenon.

VI. CONCLUSION

Using the differential method, we have calculated the electromagnetic field around metallic pads periodically distributed on a silica substrate and illuminated in TIR. This method is well adapted to periodic samples; it allows one to calculate the electromagnetic field diffracted by the sample and to build up again the images obtained for the different modes of operation: the constant height mode, the constant intensity mode, and the two-wavelength mode. As the reconstruction of the field from the Rayleigh expansion is relatively easy, the comparison is possible whatever be the experimental setpoint intensity value for our experimental results obtained in the two last modes. Our simulations in the constant height mode show that the localization of the electromagnetic field can be strongly different from the shape of the pads. By comparing these results with the field diffracted by dielectric pads with the same geometrical shape, it appears that the enhancement is more important in the case of metallic pads. For dielectric pads, the maximum intensity is localized just above the pad, whereas the ditribution of the field is more sensitive to the edges of metallic pads. Very close to the Au pad, the localization of the enhancement is issued from the discontinuity of the permittivity between the metal and the air. For the constant intensity mode, the measurements show an excellent agreement with the corresponding simulations. These results, obtained in *s* and *p* polarizations and for a probe-to-sample distance varying between 30 and 400 nm, confirm that, for the metallic sample, the intensity collected by the fiber tip (multimode fiber etched chemically and nonmetallized) is proportional to the square modulus of the electric field. The recording of a set of images in the constant intensity mode for each polarization give us the distribution of the electromagnetic field in the near-field region. However, it is not possible to determine quantitatively the effect of polarization by direct comparison of only two recorded images in each polarization. To study the effect of the polarization change, and to bypass the problem of the variation of the optical signal as a function of probe-to-sample distance, we use the so-called two-wavelength mode. This mode allows us to study the change of incident polarization, for a ''controlled'' probe-to-sample distance. During the images scanning, the reference surface enables a comparison of images obtained by changing in *s* and *p* polarizations or with various illumination parameters. The understanding of the formation of the electromagnetic field pattern above the metallic pads and the coupling with the probe tip requires one to modify in a controlled way the probe-to-sample distance in the evanescent zone. The two-wavelength mode allows one to do this. Other techniques exist to control the probe-to-sample distance. Atomic force microscopy (AFM) or ''shear force'' techniques are commonly used to regulate this distance which is generally smaller than 20 nm. The feedback of the two-wavelength mode can be regarded as a complementary feedback (AFM or shear force). One of its advantages is the possibility to choose a reference surface in the optical near-field region more or less close to the sample. This reference surface differs from the sample to-

pography and depends on the illumination conditions in a complicated way, while in the AFM or shear force technique this reference surface is related to the sample topography. However, the advantage of a such control lies in the possibility to probe the near-field of an optical phenomenon (for example, surface plasmons, fluorescence, etc.) for probe-to-sample distances such that the probe does not disturb the studied phenomenon.

*Email address: lsalomon@u-bourgogne.fr

[1] P. F. Liao, in *Surface Enhanced Raman Scattering*, edited by R. K. Chang and T. E. Furtak (Plenum, New York, 1982).
[2] P. M. Adam, L. Salomon, F. de Fornel, and J. P. Goudonnet, Phys. Rev. B **48**, 2680 (1993).
[3] P. Dawson, F. de Fornel, and J. P. Goudonnet, Phys. Rev. B **72**, 2927 (1994).
[4] J. R. Krenn, D. Somitsch, W. Gotschy, A. Leitner, and F. R. Aussenegg, Appl. Phys. A **61**, 541 (1995).
[5] D. P. Tsai, J. Kovacs, Z. Wang, M. Moskovits, V. Shalaev, J. S. Suh, and R. Botet, Phys. Rev. Lett. **72**, 4149 (1994).
[6] S. I. Bozhevolnyi, B. Vohnsen, I.I. Smolyaninov, and A.V. Zayats, Opt. Commun. **117**, 417 (1995).
[7] B. Hecht, H. Bielefeldt, L. Novotny, Y. Inouye, and D. W. Pohl, Phys. Rev. Lett. **77**, 1889 (1996).
[8] S. I. Bozhevolnyi and F. A. Pudonin, Phys. Rev. Lett. **78**, 14 (1997); **78**, 2823 (1997)
[9] E. Betzig, J. K. Trautman, J. S. Weiner, T. D. Harris, and R. Wolfe, Appl. Opt. **31**, 22 (1992); **31**, 4563 (1992).
[10] Ch. Girard, A. Dereux, O. J. F. Martin, and M. Devel, Phys. Rev. B **52**, 2889 (1995).
[11] M. Xiao, J. Opt. Soc. Am. A **14**, 2977 (1997).
[12] F. de Fornel, L. Salomon, P. M. Adam, E. Bourillot, J. P. Goudonnet, and M. Nevière, Ultramicroscopy **42-44**, 422 (1992).
[13] R. Petit, *Electromagnetic Theory of Grating* (Springer Verlag, Berlin, 1980).
[14] P. Vincent, Opt. Commun. **26**, 293 (1978).
[15] D. Maystre and M. Nevière, J. Opt. (Paris) **9**, 301 (1978).
[16] R. Carminati and J. J. Greffet, Opt. Commun. **116**, 316 (1995).
[17] D. Van Labeke and D. Barchiesi, J. Opt. Soc. Am. **10**, 2193 (1993).
[18] P. B. Johnson and R. W. Christy, Phys. Rev. B **6**, 4370 (1972).
[19] Ch. Girard, A. Dereux, O. J. F. Martin, and M. Devel, Phys. Rev. B **50**, 14 467 (1994).
[20] R. Carminati and J. J. Greffet, Opt. Lett. **21**, 1208 (1996).
[21] F. de Fornel, P. M. Adam, L. Salomon, J. P. Goudonnet, and P. Guérin, Opt. Lett. **19**, 1082 (1994).